Magnetic excitations in a cycloidal magnet: the magnon spectrum of multiferroic $TbMnO_3$

2008 J. Phys.: Condens. Matter 20 434212

(http://iopscience.iop.org/0953-8984/20/43/434212)

IOP PUBLISHING JOURNAL OF PHYSICS: CONDENSED MATTER

J. Phys.: Condens. Matter **20** (2008) 434212 (13pp) doi:10.1088/0953-8984/20/43/434212

Magnetic excitations in a cycloidal magnet: the magnon spectrum of multiferroic $TbMnO_3$

D Senff[1], N Aliouane[2], D N Argyriou[2], A Hiess[3], L P Regnault[4], P Link[5,6], K Hradil[7], Y Sidis[8] and M Braden[1]

[1] II Physikalisches Institut, Universität zu Köln, Zülpicher Straße 77, D-50937 Köln, Germany
[2] Hahn-Meitner-Institut, Glienicker Straße 100, 14109 Berlin, Germany
[3] Institut Laue-Langevin, Boîte Postale 156, 38042 Grenoble Cedex 9, France
[4] CEA-Grenoble, DRFMC-SPSMS-MDN, 17 rue des Martyrs, 38054 Grenoble Cedex 9, France
[5] Spektrometer PANDA, Institut für Festkörperphysik, TU Dresden, Germany
[6] Forschungsneutronenquelle Heinz Maier-Leibnitz (FRM II), TU München, 85747 Garching, Germany
[7] Institut für Physikalische Chemie, Universität Göttingen, Tammanstraße 6, 37077 Göttingen, Germany
[8] Laboratoire Léon Brillouin, CEA/CNRS, 91191 Gif-sur-Yvette Cedex, France

E-mail: braden@ph2.uni-koeln.de

Received 27 March 2008, in final form 7 May 2008
Published 9 October 2008
Online at stacks.iop.org/JPhysCM/20/434212

Abstract

The magnetic excitations in multiferroic $TbMnO_3$ have been investigated by inelastic scattering of polarized and unpolarized neutrons in the ferroelectric cycloidal and in the paraelectric collinear phase. The polarization analysis of the excitations at the incommensurate magnetic zone center allows one to determine the characters of three distinct modes. In particular we may identify those modes which may directly couple to the ferroelectric polarization. We find a rather complex magnon dispersion with branches split throughout the Brillouin zone, which should be a generic characteristic of elliptical cycloidal order.

(Some figures in this article are in colour only in the electronic version)

1. Introduction

The detailed understanding of the phonon dynamics of ferroelectric materials has attracted a lot of interest over the last decades, as in conventional ferroelectrics the ferroelectric transition and the divergence of the corresponding susceptibility are related to the softening of the optical phonon mode associated with the displacive structural transitions [1, 2]. In multiferroic systems with a close correlation between magnetism and ferroelectricity, the ferroelectric and the magnetic order parameters are intimately coupled, and the critical fluctuations of the ferroelectric phase are no longer of purely phononic origin, but possess a magnetic component as well. The associated low-energy excitations consist of hybridized magnon–phonon excitations, referred to as electromagnons.

Predicted almost 40 years ago [3–5], the experimental observations of hybridized phonon–magnon oscillations were, however, hampered by the weakness of the magnetoelectric effects in most compounds [6]. Only with the recent renaissance of this field and with the observation of multiferroicity in transition-metal oxides with frustrated magnetic correlations, has the investigation and characterization of these novel quantum excitations become possible. In this class of compounds, ferroelectricity is induced by a complex, non-collinear magnetic ordering [7–9], and giant magnetoelectric effects have been reported under the application of an external magnetic field [10–15]. The close coupling between magnetism and ferroelectricity in these systems opens the way to a detailed analysis of the dynamics of magnetic ferroelectrics, and the first evidence for an electromagnon excitation has been observed through an unconventional polarization depen-

dence in optical spectroscopy on multiferroic $GdMnO_3$ and $TbMnO_3$ [16, 17]. In the meanwhile similar experiments have been performed on $Eu_{0.75}Y_{0.25}MnO_3$ [18], $DyMnO_3$ [19], YMn_2O_5 and Tb_2MnO_5 [20], but the interpretation of these signals is still unclear. The main open issue concerns the fact that by far the strongest signal in the $RMnO_3$ compounds is always observed with the electric field oriented along the **a**-direction, whereas the static ferroelectric polarization can point along **a** or **c** [18] depending on the material and on the external field. One may thus wonder whether the strong infrared (IR) response is directly coupled to the multiferroic transition.

In most of the recently discovered oxide multiferroics, ferroelectricity appears to be induced by an inverse Dzyaloshinski–Moriya interaction [7–9]: for a pair of spins $\boldsymbol{S}_i$, $\boldsymbol{S}_j$ separated by a distance vector $\boldsymbol{r}_{i,j}$ the induced electric polarization is given by

$$\boldsymbol{P} \propto \boldsymbol{r}_{ij} \times (\boldsymbol{S}_i \times \boldsymbol{S}_j), \tag{1}$$

and the appearance of a finite electric polarization is correlated with complex non-collinear magnetic ordering [15, 21–24]. As a consequence, the magnetic excitation spectrum consists of numerous magnon branches, and the identification of the magnetic part of the electromagnon excitation requires a comprehensive analysis.

Best suited for the investigation of the spin-wave spectrum in the ferroelectric cycloidal phase is the manganite compound $TbMnO_3$—one of the key materials in the family of multiferroic oxides [10, 25]. Similar to the parent compound of the rare-earth manganites $LaMnO_3$, $TbMnO_3$ crystallizes in the orthorhombic symmetry of space group $Pbnm$ with room-temperature lattice constants $a = 5.302$ Å, $b = 5.857$ Å and $c = 7.402$ Å [26, 27], which in the following will be used to index vectors in reciprocal space. However, due to the smaller size of the rare-earth ion the typical structural distortions of the $GdFeO_3$-type are strongly enhanced in the case of $TbMnO_3$, resulting in the suppression of the commensurable A-type magnetic order as the magnetic ground state [28]. Instead, upon cooling, three different magnetic phase transitions can be identified in $TbMnO_3$ [29]: below $T_N = 42$ K a collinear spin-density wave order (SDW) with the Mn spins aligned along $\boldsymbol{b}$ and propagation vector $\boldsymbol{k}_{SDW} \approx (0, 0.28, 0)$ is stabilized [21, 29, 30], see figure 1(a). At lower temperatures a reorientation in the Mn subsystem is observed, and below $T_{FE} = 28$ K the Mn moments order in a cycloid structure with the spins confined to the $\boldsymbol{bc}$ plane, spin chirality $\mathcal{C} = \boldsymbol{S}_i \times \boldsymbol{S}_{i+1} \parallel \boldsymbol{a}$ and propagation vector $\boldsymbol{k}_{cycl} \approx (0, 0.28, 0)$ similar to the SDW phase [21], see figure 1(b). The third magnetic transition at $T_{Tb} = 7$ K is attributed to the ordering of the Tb moments [29, 30].

Simultaneously with the transition into the cycloid phase, a spontaneous electric polarization $\boldsymbol{P}_c$ along $\boldsymbol{c}$ appears in zero magnetic field [10], which is well explained on the basis of the Dzyaloshinski–Moriya formalism described by equation (1) [7, 8]. Applying a magnetic field, giant magnetoelectric effects are observed; a critical field $\boldsymbol{H}_c = 7$ T along $\boldsymbol{c}$ completely suppresses the electric polarization [25, 31], while a field of 10.5 T (6 T) parallel to $\boldsymbol{a}$ ($\boldsymbol{b}$) flips the electric polarization by 90° from $\boldsymbol{P}_c$ to $\boldsymbol{P}_a \| \boldsymbol{a}$ [10, 25] most likely due to a flip of the cycloidal basal plane [45].

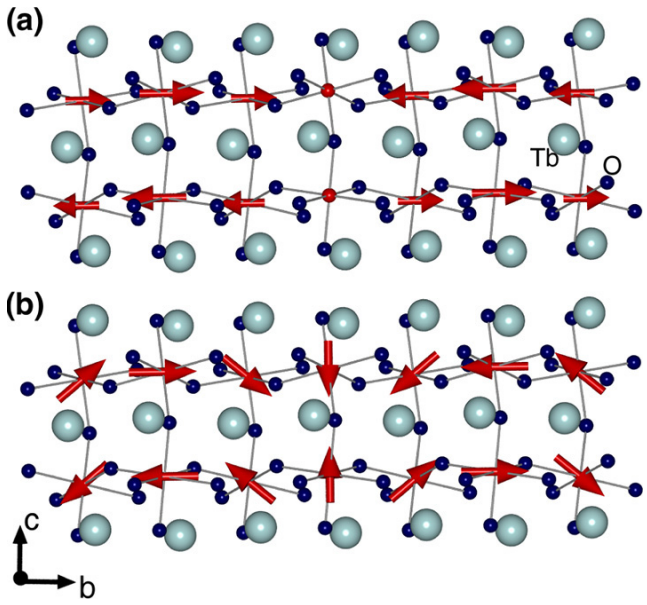

Figure 1. Cut through the $\boldsymbol{bc}$ plane of the orthorhombic crystal structure in $TbMnO_3$ showing (a) the spin-density wave ordering of the Mn spins in the paraelectric phase below $T_N = 42$ K, and (b) the cycloid ordering in the ferroelectric phase below $T_{FE} = 28$ K. The magnetic correlations along $\boldsymbol{a}$ not included in the sketch are always ferromagnetic.

In this article we will present our inelastic neutron scattering results on the magnetic excitation spectrum in multiferroic $TbMnO_3$. We discuss the spin-wave excitations in the ferroelectric cycloidal as well as in the paraelectric SDW phase, analyzing the characters of the different magnon branches. Thereby we may identify those excitations in the ferroelectric and in the paraelectric phase which possess the symmetry of the electromagnon. The most important results were already published in a letter [32] revealing the good agreement between the energies of the magnetic zone-center excitations and the peaks in the IR signal. The article is organized as follows. Following section 1, section 2 summarizes the experimental details. In section 3 we characterize the excitation spectrum at the magnetic zone center, first for the ferroelectric phase and then for the collinear SDW phase. In section 4 we extend the analysis of the zone-center modes and consider the dispersion of the different magnon branches in order to discuss the strength of the competing magnetic exchange interactions in $TbMnO_3$. Section 5 presents a discussion of the interpretation of the IR response in the $RMnO_3$ materials followed by a concluding summary.

2. Experimental details

The experiments on the magnetic excitation spectrum in $TbMnO_3$ have been performed on the thermal triple-axis spectrometers PUMA and 1T.1 installed at the FRM II in Munich and at the Laboratoire Léon Brillouin (LLB) in Saclay,

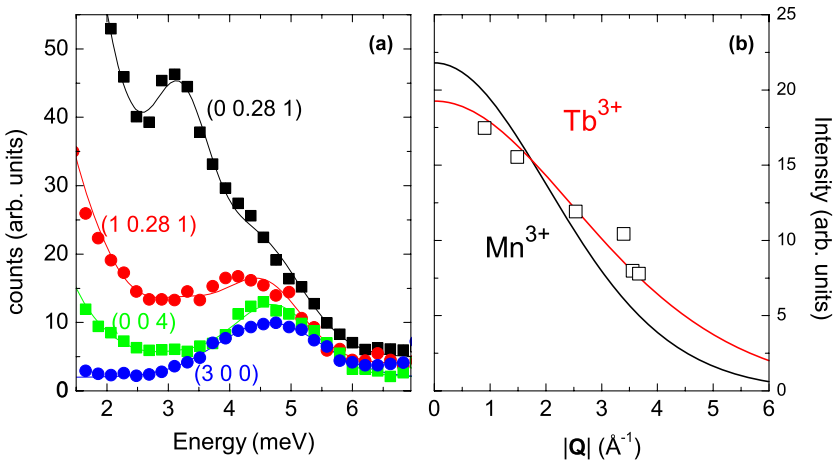

Figure 2. (a) Energy scans at different Q-positions for $T = 4.5$ K. The Tb-CEF excitation is visible around 4.5 meV in all scans, the scans at small $|Q|$ are, however, dominated by the inelastic scattering from the Mn subsystem, see the discussion in the text. (b) Q-dependence of the spectral intensity of the CEF excitation. Solid lines denote the expected suppression of the signal according to the Mn and Tb form factor [36], respectively.

respectively, and at the cold spectrometers PANDA at the FRM II, 4F.2 at the LLB and IN14 at the ILL in Grenoble. For all experiments we used the same large single crystal as in our previous studies [32, 33]. In most of the experiments the crystal was mounted with the scattering plane defined by the directions [0 1 0] and [0 0 1]; although to study the magnon dispersion along a we used a different mounting with the direction [0 2 1] perpendicular to the scattering plane, so that in this setting reflections of the kind (h 0.28 1) were easily accessible without tilting the sample. In the experiments using unpolarized neutrons the (002)-reflection of pyrolytic graphite was used to monochromate and analyze the energy of the neutrons, whereas we used the (111)-reflection of a Heusler crystal as an analyzer in the case of the polarization studies at the IN14 spectrometer. Typically, the energy of the analyzed neutrons was fixed to 4.66 meV on the cold machines, and to 8.04 or 14.7 meV on the thermal instruments. To suppress contamination by higher order neutrons, an appropriate filter, either pyrolytic graphite or cooled beryllium, was installed behind the sample in the neutron path. The polarization analysis at the IN14 spectrometer was acquired using the CRYOPAD device, allowing a precise control of the neutron's spin quantization axis.

3. Magnetic excitation spectrum at the magnetic zone center

The determination of the low-energy part of the magnetic excitation spectrum in $TbMnO_3$ is severely hampered by a low-lying crystal field excitation (Tb-CEF), which also contributes to the neutron scattering cross section and which interferes with the magnon intensities [32, 34]. In figure 2(a) we show representative energy scans at different Q-positions for $T = 4.5$ K. In all spectra a pronounced peak is detectable around 4.5 meV, which seems not to depend explicitly on Q, and which is visible at temperatures well above the Néel ordering of the Mn subsystem at $T_N = 42$ K (data not shown). Refining this feature using the ResLib code [35], we obtain the relative spectral weight of the excitation at 4.5 meV for the different Q positions, which is shown in figure 2(b). The suppression of the spectral intensity with increasing $|Q|$ perfectly follows the predictions set by the Tb^{3+} form factor, whereas the agreement with the form factor of Mn^{3+} is poor [36]. Hence, we attribute this feature to an excitation of the Tb subsystem, and as no dispersion or significant temperature dependence can be observed, we identify it with a low-lying Tb crystal field excitation [37] in agreement with [30]. Since we are primarily interested in the spin-wave excitations of the Mn subsystem, we will ignore this feature in the following.

3.1. Magnon excitations in the ferroelectric cycloid phase

Figure 3(a) presents the spin-wave spectrum at the antiferromagnetic zone center $Q = (0, 0.28, 1)$ in the ferroelectric spiral phase at $T = 17$ K, recorded using unpolarized neutrons. In addition to the elastic contribution at $E = 0$ meV different well resolvable spin-wave signals are visible around $\hbar\omega_{\perp_1} \approx 1.0$ meV and $\hbar\omega_{\perp_2} \approx 2.5$ meV in the energy range below the Tb-CEF excitation at 4.5 meV. Also depicted in figure 3(a) is the experimental resolution of the spectrometer at the elastic position $E = 0$ meV as determined with a vanadium standard sample. Close to the elastic line, the observed spectrum significantly deviates from the expected behavior for a purely elastic contribution, thus signaling a third, soft inelastic contribution $\omega_\parallel$ below 0.5 meV. Indeed, the observed spectrum can best be fitted assuming two Gaussian-shaped excitations representing two-magnon excitations $\omega_{\perp_{1,2}}$ at finite energies, and a strongly overdamped harmonic oscillator representing the third soft mode $\omega_\parallel$ at low energies, see figure 3(a).

To further quantify the above analysis and to characterize the excitation spectrum in the ferroelectric cycloid phase of $TbMnO_3$ in more detail we have extended our studies to the use of polarized neutrons, see the inset figure 3(b). In the classical longitudinal neutron polarization analysis six different scattering cross sections can be measured: for

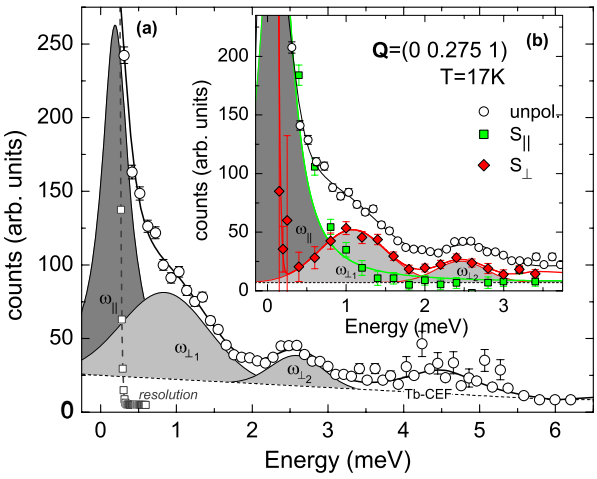

Figure 3. (a) Magnetic excitation spectrum at the antiferromagnetic zone center $\boldsymbol{Q} = (0, 0.275, 1)$ in the ferroelectric spiral phase for $T = 17$ K recorded using unpolarized neutrons. Solid lines denote fits to the data, and shaded areas mark the different magnon signals, see the text. Open squares and dashed lines correspond to the experimental resolution determined using a vanadium standard sample. (Inset, b) polarization analysis of the excitation spectrum with the decomposition of the unpolarized spectrum into the components of the dynamic magnetization parallel and perpendicular to the $\boldsymbol{ab}$ spiral plane, $S_\parallel$ and $S_\perp$, respectively.

each $\boldsymbol{Q}$-value the neutron spin can be aligned along three orthogonal directions parallel to the scattering vector $\boldsymbol{Q}$ (x), perpendicular to $\boldsymbol{Q}$ and within the scattering plane (y), and perpendicular to both $\boldsymbol{Q}$ and the scattering plane (z). This technique gives rise to three spin-flip (SF) and three non spin-flip (NSF) intensities. The polarization analysis adds an additional selection rule to the general neutron scattering law that only magnetic components perpendicular to the scattering vector $\boldsymbol{Q}$ contribute: in the spin-flip channel the magnetic polarization must be perpendicular to the neutron polarization. Combining the different cross sections allows one to reconstruct the components of the magnetization $S_\parallel$ parallel and $S_\perp$ perpendicular to the scattering plane [38], which in our case with $\boldsymbol{a}$ vertical yields the magnetic fluctuations polarized parallel and perpendicular to the $\boldsymbol{bc}$ spiral plane of the magnetic structure.

The comparison with the unpolarized spectrum nicely highlights how the spectrum decomposes into the different contributions. The two modes at finite energies $\omega_{\perp_{1,2}}$ both contribute only in the $S_\perp$ channel, whereas the soft mode $\omega_\parallel$ can only be detected in the channel $S_\parallel$, see figure 3(b). With $\boldsymbol{a}$ vertical to the scattering plane, the two modes at finite energy thus correspond to magnetic fluctuations along $\boldsymbol{a}$, i.e. perpendicular to the basal plane of the helical structure, while the third mode at low energies describes a magnetic oscillation within the cycloid basal plane, i.e. the $\boldsymbol{bc}$ plane.

The two excitations $\omega_{\perp_{1,2}}$ appear well separated in the $S_\perp$ spectrum, as there is no overlap with the low-energy mode, but the interpretation of the data is intriguing. We obtain the frequencies $\hbar\omega_{\perp_1} = 1.07(5)$ meV and $\hbar\omega_{\perp_2} = 2.50(8)$ meV. In addition to the inelastic features a sharp signal is found at the elastic position for $S_\perp$ arising from the finite neutron polarization. Taking the exact value of the finite flipping ratio into account, $I_{\mathrm{NSF}}{:}I_{\mathrm{SF}} = 35$ determined on a structural Bragg reflection, we find a fully vanishing ordered moment along **a** in agreement with the unpolarized diffraction experiments [21]. The $S_\parallel$-spectrum consists of a single broad contribution centered around the elastic position $E = 0$ meV. However, the tail of the signal extends up to 1 meV, which is significantly broader than the experimental resolution $\Delta E \approx 0.125$ meV, and has to be attributed to a low-energy soft mode. We emphasize that a similar signal is absent in the other channel. The frequency of this overdamped excitation can be estimated to $\omega_\parallel = 0.11(5)$ meV.

To analyze the different characters of the three magnetic excitations we consider in the following a circular cycloidal structure with a constant vector chirality $\mathcal{C} = \boldsymbol{S}_i \times \boldsymbol{S}_j$ along $\boldsymbol{a}$, propagation vector $\boldsymbol{k}_{\mathrm{cycl}} \| \boldsymbol{b}$ and amplitude S_0. Note, however, that the real magnetic structure in $TbMnO_3$ is elliptical which may render the excitation spectra even more complex. The static moment at the site $\boldsymbol{r}_i$ is given by:

$$\boldsymbol{S_i} = S_0 \cdot \cos(\boldsymbol{k}_{\mathrm{cycl}} \cdot \boldsymbol{r}_i)\boldsymbol{e_b} + S_0 \cdot \sin(\boldsymbol{k}_{\mathrm{cycl}} \cdot \boldsymbol{r}_i)\boldsymbol{e}_{\mathrm{c}}. \qquad (2)$$

In order to discuss the magnetoelectric relevance of the different magnon modes it appears convenient to analyze the magnetic structure resulting from a freezing-in of the respective magnon modes. This analysis can be performed for the paraelectric SDW phase as well as for the multiferroic cycloidal phase. The phason or sliding mode of the cycloid is one possible low-energy excitation polarized within the rotational $\boldsymbol{bc}$ plane. It is associated with a transversal magnetic fluctuation of the local moment around the rotation axis $\boldsymbol{a}$: the phason mode alters the phase of the cycloid with respect to the underlying crystal lattice, but it leaves the relative orientation of the spin system unchanged. In consequence the phason mode should not possess a finite energy for an ideal cycloidal order. The associated polarization scheme at the magnetic zone center $\boldsymbol{Q} = \boldsymbol{k}_{\mathrm{cycl}}$ is sketched in figure 4(a). Since the sliding mode does not alter the spin chirality $\mathcal{C}$, this mode is decoupled from the electric polarization and it does not possess an electromagnon character. A longitudinal spin excitation in the high-moment ordered structure should possess a considerably higher energy, so that we may identify the observed $\boldsymbol{bc}$-polarized mode $\omega_\parallel$ as the phason. Its finite, but still low frequency, may arise from the pinning of the incommensurable magnetic structure as well as from small magnetic anisotropies combined with the asymmetry of the static order, which is elliptical rather than circular in the case of $TbMnO_3$ [21].

Next we discuss the different characters of the two $\boldsymbol{a}$-polarized modes $\omega_{\perp_{1,2}}$, which induce a time dependent magnetization $S_i^a(\boldsymbol{q}, \omega)$ along $\boldsymbol{a}$ at the site $\boldsymbol{r}_i$:

$$S_i^a(\boldsymbol{q} = 0, \omega) = S_0^a \cos(\boldsymbol{k}_{\mathrm{cycl}}\boldsymbol{r}_i + \delta) \cdot \cos(\omega t). \qquad (3)$$

The fluctuation necessarily possesses the same wavelength as the static spin structure, but the oscillations can be either in-phase with the static $\boldsymbol{b}$ component, $\delta = 0$ and cosinusoidally modulated, or in-phase with the static $\boldsymbol{c}$ component, $\delta = \frac{\pi}{2}$ and sinusoidally modulated. The arising polarization patterns are distinct as is shown in figures 4(b) and (c).

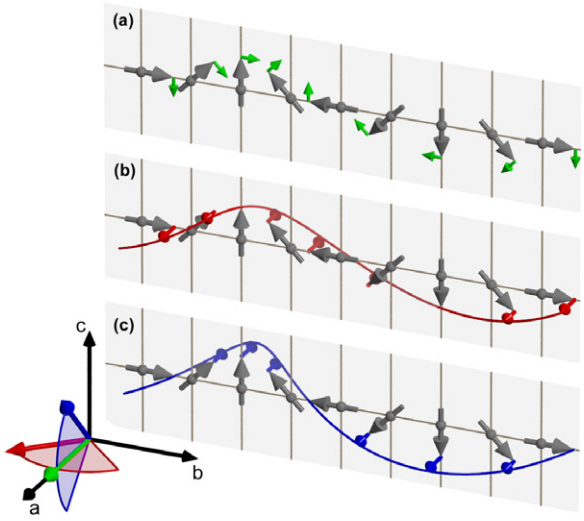

Figure 4. Sketch of the polarization schemes of the different magnon excitations at the magnetic zone center of the cycloid structure as described in the text. The static spin structure is marked by thick gray, and the local fluctuations by smaller colored arrows. In addition, the spin chirality $\mathcal{C} = \boldsymbol{S}_i \times \boldsymbol{S}_{i+1}$ is shown for the sketched instantaneous spin arrangement with the different modes marked by the color scheme. The $\boldsymbol{bc}$-polarized sliding mode can be regarded as a rotation of the spin plane around $\boldsymbol{a}$ (a). For the $\boldsymbol{a}$-polarized modes the fluctuations can either be in-phase with the static $\boldsymbol{b}$-component (b), or with the static $\boldsymbol{c}$-component (c), resulting in a rotation of the spiral plane around $\boldsymbol{c}$ and $\boldsymbol{b}$, respectively. In the lower-left edge we show the vector diagram of the ferroelectric oscillating polarization associated with the three magnons.

For small amplitudes S_0^a we can evaluate the central equation (1) for the excited state at $\boldsymbol{q} = 0$, and obtain with $\varphi_0 = \boldsymbol{k}_{\rm cycl}\boldsymbol{r}_{i,i+1}$ denoting the phase difference between adjacent sites for the cosinusoidal mode

$$(\boldsymbol{S}_i \times \boldsymbol{S}_{i+1})^{\cos} = S_0(S_0 \sin(\varphi_0), S_0^a \sin(\varphi_0) \cdot \cos(\omega t), 0), \quad (4)$$

and for the sinusoidally modulated $\frac{\pi}{2}$ mode:

$$(\boldsymbol{S}_i \times \boldsymbol{S}_{i+1})^{\sin} = S_0(S_0 \sin(\varphi_0), 0, S_0^a \sin(\varphi_0) \cdot \cos(\omega t)). \quad (5)$$

Hence, both modes alter the basal plane of the cycloid; while the cosinusoidal mode rotates the spin plane around $\boldsymbol{c}$, the sinusoidal fluctuation rotates it around $\boldsymbol{b}$, as is shown in the inset of figure 4.

Since the propagation vector, or $\boldsymbol{r}_{i,j}$ in equation (1), always remains along $\boldsymbol{b}$, the rotation of the spin chirality $\boldsymbol{S}_i \times \boldsymbol{S}_{i+1}$ around $\boldsymbol{b}$ through the $\frac{\pi}{2}$-magnon gives rise to a strong linear coupling to the electric polarization [39]. This excitation can be considered as the electromagnon of the multiferroic phase, because the magnon excitation is associated with the oscillation of the electric polarization along $\boldsymbol{a}$. Neglecting the finite energy of this excitation due to single-ion anisotropies, this mode furthermore can be associated with the Goldstone boson of the ferroelectric phase [39]. The second transverse magnon oscillates the angle between $\mathcal{C}$ and $\boldsymbol{k}_{\rm cycl}$ and couples only quadratically, and thus weakly, to the dynamic electric polarization. It yields a marginal modulation of the static polarization along $\boldsymbol{c}$. With the polarization analysis we, however, may not distinguish the two $\boldsymbol{a}$-polarized modes, whose characters may further mix due to deviations from the ideal cycloidal ordering.

In optical spectroscopy, evidence for an electromagnon response has recently been reported by Pimenov *et al* in the multiferroic phase of $TbMnO_3$ [16]. The IR experiment reveals an unconventional absorbtion for the electric field of the incoming light polarized along $\boldsymbol{a}$, which can be suppressed by an applied external magnetic field and which is interpreted as an electrically active magnetic excitation: the electromagnon. The energy and the polarization of the dominant peak in the IR feature are in perfect agreement with the magnon frequencies of our neutron scattering experiments and the analysis of the magnetic excitations in a cycloid structure [39]. For $T = 12$ K Pimenov *et al* report a peak frequency $\nu = 20\ \mathrm{cm}^{-1} = 2.48$ meV for the electromagnon excitation [16], which perfectly matches the energy of the magnon excitation $\omega_{\perp_2}$ revealed in the neutron scattering data, but the total optical response appears to be much broader than the magnon mode. It is thus tempting to interpret the $\omega_{\perp_2}$ mode as the hybridized magnon–phonon excitation predicted to exist in magnetic ferroelectrics long ago [3, 4]: the optical study probes the lattice part, while the polarized neutron scattering investigation is sensitive to the magnetic channel of the hybridized excitation.

An identification of the electromagnon with the $\omega_{\perp_{1,2}}$ mode bases on the interpretation of the IR results. That the peak in the IR feature indeed corresponds to the electromagnon defined as a coupling of one phonon and one magnon, however, is not fully ascertained, see section 5. According to the above analysis, the electromagnon is also associated with the rotation of the electric polarization around $\boldsymbol{b}$. One might expect this mode to be rather low in energy, as a modest magnetic field $\boldsymbol{H}_{a,b}$ flips the electric polarization by 90° from $\boldsymbol{P}_c$ to $\boldsymbol{P}_a$ in $TbMnO_3$ [10, 25]. However, a weaker feature is seen in the IR-spectroscopy results around $10\ \mathrm{cm}^{-1} = 1.24$ meV, which exhibits the same unconventional behavior as the dominant peak at $20\ \mathrm{cm}^{-1}$. The frequency of the lower IR feature agrees with the energy of the magnon excitation $\omega_{\perp_1}$ suggesting that this mode has electromagnetic character as well. The strict separation between the two different $\boldsymbol{a}$ polarized spin-wave modes as described above is only valid for a perfect circular cycloid. In the realistic case of an elliptic structure [21] this strict separation will not hold any longer and both modes might slightly mix, rendering both magnon excitations IR active.

3.2. Spin-wave spectrum in the paraelectric spin-density wave phase

Next, we focus on the magnetic excitations in the spin-density wave phase [10, 40, 41]. Although the collinear magnetic order does not induce a static electric polarization, the analysis of the spin-wave spectrum reveals electromagnon excitations even in the paraelectric phase and allows one to identify the soft mode of the ferroelectric transition.

The magnetic excitation spectrum in the SDW phase for $T = 32$ K at the magnetic zone center $\boldsymbol{Q} = (0, 0.28, 1)$ is shown in figure 5(a). Comparing the unpolarized spectrum in

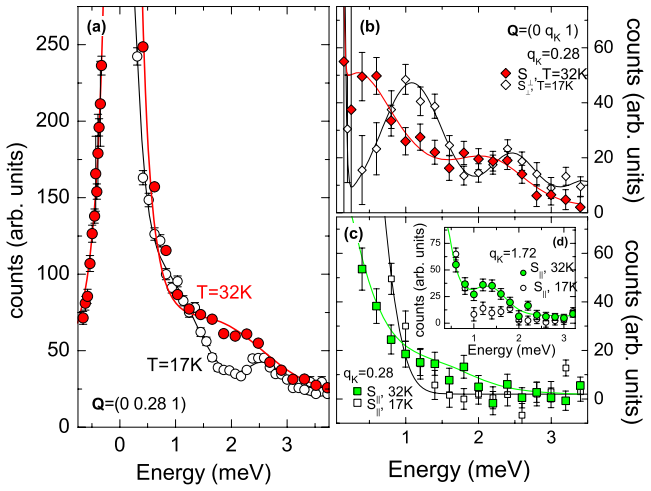

Figure 5. Comparison of the energy scan at the magnetic zone center $\boldsymbol{Q} = (0, 0.28, 1)$ in the ferroelectric cycloid phase at $T = 17$ K, and in the paraelectric SDW phase at $T = 32$ K: (a) superposition of both components, (b) the components perpendicular to the $\boldsymbol{b}$, c plane, and (c) the components parallel to the $\boldsymbol{b}$, c plane. The inset in (c) shows the parallel component at $\boldsymbol{Q} = (0, 1.72, 1)$.

the SDW phase with that of the ferroelectric cycloid phase, the spectrum is less structured and only a single broad contribution centered around 2.0 meV can be resolved. Again, close to the elastic line the response is significantly broadened, which signals an additional inelastic contribution below ≈0.5 meV. However, the use of polarized neutrons allows us to identify at least four different magnon modes in the SDW phase, which all contribute to the broad response in an unpolarized study, see figure 5.

We start with the discussion of the $S_\perp$-channel, i.e. with the magnetic fluctuations along $\boldsymbol{a}$. Similar to the cycloid phase, two distinct excitations are distinguishable in the $S_\perp$-channel at $\boldsymbol{Q} = (0, 0.28, 1)$. However, the energy of both branches is reduced compared to the 17 K data, as we find $\hbar\omega_1^a = 0.31(9)$ meV and $\hbar\omega_2^a = 2.16(10)$ meV for the two $\boldsymbol{a}$-polarized branches.

At the same $\boldsymbol{Q}$ position, the $S_\parallel$ signal is dominated by an intense inelastic contribution close to the elastic line, see figure 5(c). However, the comparison with the spectrum at 17 K suggests an additional fourth magnon mode centered around ≈1.5 meV, as the inelastic intensity is increased around this energy transfer in the SDW phase. Further support for a second inelastic contribution to $S_\perp$ is given by the spectrum recorded at the equivalent magnetic Bragg position $\boldsymbol{Q} = (0, 1.72, 1)$, in which the signal around 1.5 meV also appears enhanced, whereas it is clearly absent in the cycloid phase at $T = 17$ K. Combining the spectra at both $\boldsymbol{Q}$ positions we obtain the energies $\hbar\omega_1^{bc} = 0.10(8)$ meV and $\hbar\omega_2^{bc} = 1.32(8)$ meV for the overdamped soft mode and for the finite-energy mode in the $S_\parallel$ channel, respectively.

With $\boldsymbol{a}$ vertical to the scattering plane, the $S_\parallel$ channel measures the magnetization within the $\boldsymbol{bc}$ plane [38]. However, in magnetic neutron scattering only the component of the magnetization perpendicular to the scattering vector $\boldsymbol{Q}$ contributes to the cross section, which superimposes the particular laws for the scattering of polarized neutrons [42]. With the different choices of the scattering vector we significantly modify the magnetic structure factor, as for $\boldsymbol{Q}_1 = (0, 0.28, 1)$ the scattering vector includes an angle of 19.49° with $\boldsymbol{c}$, whereas $\boldsymbol{Q}_2 = (0, 1.72, 1)$ and $\boldsymbol{c}$ span an angle of 65.29°. Taking the orthogonal complement from the projections onto $\boldsymbol{c}$ for $\boldsymbol{Q}_1$ and $\boldsymbol{Q}_2$ and correcting for the different magnetic form factors [36], the expected intensity ratio for a $\boldsymbol{c}$-polarized fluctuation is $I_{Q_1}{:}I_{Q_2} = 1{:}4.99$, which is in fair agreement with the observed distribution of spectral weight for the mode ω_2^{bc}, $I_{Q_1}^{\rm obs}{:}I_{Q_2}^{\rm obs} = 1{:}4.29(82)$. Hence, the branch $\omega_2^{bc} = 1.32$ meV represents a transverse magnetic oscillation along $\boldsymbol{c}$. Due to the strong overlap with the elastic line and the resulting uncertainties in the determination of the spectral weight a similar analysis is, unfortunately, not possible for the low-energy mode ω_1^{bc}.

In order to examine the origin of the different spin-wave modes in the SDW phase we follow the argument applied for the cycloidal phase. In the spin-density wave structure with modulation $\boldsymbol{k}_{\rm SDW}$ and the moments aligned along $\boldsymbol{b}$, the spin $\boldsymbol{S}_i$ at the site $\boldsymbol{r}_i$ is described by:

$$\boldsymbol{S}_i = S_0 \cos(\boldsymbol{k}_{\rm SDW}\boldsymbol{r}_i)\boldsymbol{e}_{\rm b}, \tag{6}$$

where the static phase is set to zero. At the magnetic zone center six different magnon modes are expected, two longitudinal modes corresponding to magnetic fluctuations along $\boldsymbol{b}$, and four transversal ones.

Let us first discuss the longitudinal modes in more detail. In a conventional magnet longitudinal modes do not exist in linear spin-wave theory [43], but the incommensurable character of the SDW ordering might activate them in our case. At the magnetic zone center $\boldsymbol{q} = 0$ a sinusoidal magnetic oscillation along $\boldsymbol{b}$ possesses the same wavelength as the static modulation, but it can be either in-phase, or out-of-phase with the ordered structure. The latter case corresponds to the phason mode of the SDW structure, as it oscillates the phase δ of the magnetic structure with respect to the underlying crystal lattice. Similar to the sliding mode of the cycloid the energy of this excitation is determined by the pinning potential of the incommensurate structure and is expected to be very low. The longitudinal in-phase mode is the 'amplitudon' of the SDW structure; it yields an oscillation of the amplitude of the local moment around the mean value. In principle, such a mode can also exist in simple commensurate magnetic structures, but it is expected to be very hard and we do not consider it to contribute in the low-energy regime we are interested in.

Now we turn our attention to the four transversal branches, which can be divided into two different groups, according to their relative phase shift with respect to the static structure: similar to the longitudinal modes the sinusoidal transverse oscillations can be either in-phase, or out-of-phase with the static structure. At the magnetic zone center the two in-phase modes retain a collinear spin arrangement. These modes correspond to the canting of the magnetic moment along the $\boldsymbol{a}$ and the $\boldsymbol{c}$ direction, respectively, thereby changing the purely longitudinal character of the SDW into a partially transversal one. For $\boldsymbol{q} = 0$ both modes test the effective magnetic anisotropy Λ_i along $\boldsymbol{a}$ and $\boldsymbol{c}$, and are therefore expected

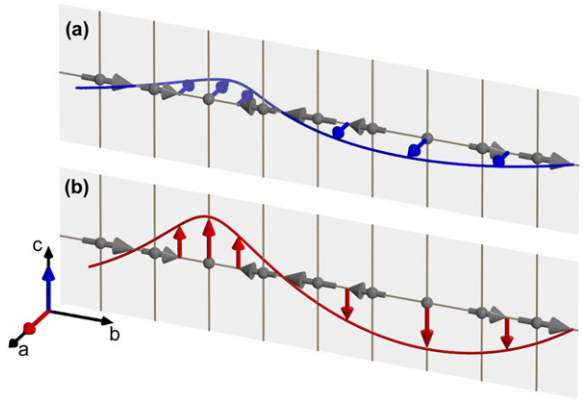

Figure 6. Polarization schemes of the two $\frac{\pi}{2}$-modes in a SDW structure. The $\boldsymbol{a}$-polarized mode transforms the SDW into a magnetic cycloid constrained to the $\boldsymbol{ab}$ plane (a), while the $\boldsymbol{c}$-polarized mode results in a $\boldsymbol{bc}$ cycloidal structure (b). In the lower-left corner the vector product $\boldsymbol{S}_i \times \boldsymbol{S}_{i+1}$ is shown for the frozen-in states with the different modes marked by the color code.

to possess a finite energy. The two in-phase modes, one polarized along $\boldsymbol{a}$ and one along $\boldsymbol{c}$, are irrelevant for the ferroelectric transition and the multiferroic coupling, as the cross product between adjacent spins always vanishes in the collinear arrangement.

In contrast, the two out-of-phase or $\frac{\pi}{2}$-modes are relevant for the ferroelectric transition and may couple to an electric polarization even in the paraelectric phase, see also [44]. The polarization schemes of these two modes are shown in figure 6. Both modes transform the SDW structure into a cycloid—for the $\boldsymbol{a}$ polarized mode the cycloid is constrained to the $\boldsymbol{ab}$ plane, while the $\boldsymbol{c}$ mode results in a $\boldsymbol{bc}$ cycloid. To determine the coupling of these modes to an electric field we evaluate equation (1) for the frozen-in modes, and obtain with φ_0 denoting the phase difference between neighboring sites

$$(\boldsymbol{S}_i \times \boldsymbol{S}_{i+1})^{\text{a-pol}} = (0, 0, \sin(\varphi_0))S_0 S_0^a \cos(\omega t) \qquad (7)$$

and

$$(\boldsymbol{S}_i \times \boldsymbol{S}_{i+1})^{\text{c-pol}} = (\sin(\varphi_0), 0, 0)S_0 S_0^c \cos(\omega t) \qquad (8)$$

for the $\boldsymbol{a}$ and $\boldsymbol{c}$ polarized mode, respectively. Hence, as $\boldsymbol{k}_{\text{SDW}} \| \boldsymbol{b}$ the $\boldsymbol{a}$-mode couples to an electric polarization $\boldsymbol{P}_a$ along $\boldsymbol{a}$ and the $\boldsymbol{c}$-mode to $\boldsymbol{P}_c$ along $\boldsymbol{c}$, even in the paraelectric phase [44]. Close to T_{FE} both modes are expected to be very low in energy, since these modes are directly associated with the phase transition into the ferroelectric phase. In zero field, the $\boldsymbol{bc}$ cycloid emerges in $TbMnO_3$ and the $\frac{\pi}{2}$-mode along $\boldsymbol{c}$ is the associated magnetic soft mode. Since the transition from the SDW to the cycloidal order is essentially continuous, the corresponding susceptibility associated with $\frac{1}{\omega^2}$ must diverge and the magnon frequency almost vanish close to the transition. The $\frac{\pi}{2}$-mode along $\boldsymbol{a}$ will be slightly harder; we recall, however, that a modest magnetic field stabilizes the $\boldsymbol{ab}$-cycloid and flips the electric polarization [24, 45]. The energies of both $\frac{\pi}{2}$-modes associated with the different orientations of the cycloid are, therefore, expected to be comparable.

An overview of the possible zone-center magnons is given in table 1. The two $\boldsymbol{a}$-polarized modes can easily be identified

Table 1. Overview of the possible magnetic excitations in the collinear SDW arrangement summarizing the polarization pattern, the phase with respect to the static ordering, the expected frequency, and the possible coupling to a varying electric field of the various modes. For more details see the text.

		Polar.	Phase	Frequency	Hybridized
Phason	ω_1^b	$\parallel \boldsymbol{b}$	$\frac{\pi}{2}$	Soft	No
Amplitudon	ω_2^b	$\parallel \boldsymbol{b}$	0	Hard	No
$\boldsymbol{ac}$-cycloid	ω_1^a	$\parallel \boldsymbol{a}$	$\frac{\pi}{2}$	Soft 0.3 meV	Yes
$\boldsymbol{a}$-canting	ω_2^a	$\parallel \boldsymbol{a}$	0	Λ_a 2.16 meV	No
$\boldsymbol{bc}$-cycloid	ω_1^c	$\parallel \boldsymbol{c}$	$\frac{\pi}{2}$	Soft	Yes
$\boldsymbol{c}$-canting	ω_2^c	$\parallel \boldsymbol{c}$	0	Λ_c 1.32 meV	No

with the two-magnon excitations $\omega_{1,2}^a$ observed in the $S_\perp$ channel. Following the above argument the mode ω_2^a at 2.16 meV is the $\boldsymbol{a}$ canting mode, and the mode ω_1^a at 0.31 meV is the $\boldsymbol{ab}$-cycloid mode. In a SDW phase one may expect the $\frac{\pi}{2}$ modes to possess lower frequencies, as they sense a smaller effective moment. The $\boldsymbol{ab}$-cycloid mode is coupled to an electric polarization and should be visible in IR-spectroscopy as well, in agreement with the work by Pimenov *et al* [16] who found the electromagnon IR response also in SDW phase. For an electric field of the incident light along $\boldsymbol{a}$ these authors also report an electromagnon response in the paraelectric phase above T_{FE}, which is shifted to lower energies compared to the ferroelectric phase, consistent with the observations in the neutron experiment. We emphasize once more, that a one-phonon one-magnon coupled electromagnon mode is not restricted to the cycloidal phase but it may also exist in a SDW phase [44] in contrast to arguments used in [19].

The four remaining spin-wave excitations at the zone center of the SDW structure should all contribute in the $S_\parallel$ channel. The amplitudon is, however, not observable in the energy range we are interested in. Comparing the inelastic response at two different $\boldsymbol{Q}$ positions we have demonstrated that the mode ω_2^{bc} at 1.32 meV corresponds to a transversal fluctuation along $\boldsymbol{c}$. This mode is the canting mode along $\boldsymbol{c}$. As in $TbMnO_3$ the hard magnetic axis is along $\boldsymbol{a}$, the energy of this mode is smaller than that of the corresponding canting along $\boldsymbol{a}$, ω_2^a. The phason mode of the SDW structure and the $\boldsymbol{bc}$-cycloid mode are both expected to be soft, and hence, we identify the observed low-energy signal ω_1^{bc} with the superposition of these two. With the finite-energy resolution of the triple-axis spectrometer we can not separate these modes. As in zero field the $\boldsymbol{bc}$-cycloid is stabilized [21], the associated excitation should be lower in energy than the equivalent $\boldsymbol{a}$-polarized excitation, consistent with the observed energy scheme. Similar to the mode ω_1^a, the cycloid excitation ω_1^{bc} also couples to an electric field, but in this case the electric polarization must point along $\boldsymbol{c}$. Further IR experiments with the electric field applied along $\boldsymbol{c}$ are highly desirable.

4. q-dependence of the magnetic excitations

So far we have discussed the magnetic excitation spectrum at the magnetic zone center $\boldsymbol{q} = \boldsymbol{0}$, which allowed us to identify the different spin-wave modes in the ferroelectric cycloid and in the paraelectric SDW phase. In this section we will

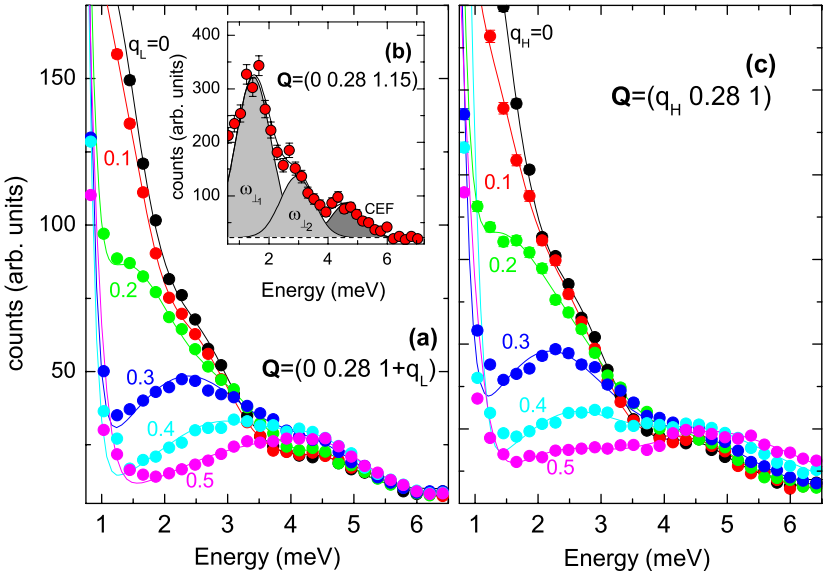

Figure 7. Raw-data energy scans at selected positions $\boldsymbol{Q} = (0, 0.28, 1 + q_l)$ ((a), (b)) and $\boldsymbol{Q} = (q_h, 0.28, 1)$ (c) to determine the magnon dispersion along $\boldsymbol{a}$ and $\boldsymbol{c}$ in the ferroelectric cycloid phase at $T = 23$ K. Data in (a) and (c) are recorded with a thermal spectrometer, those in (b) on a cold instrument with considerably increased energy resolution. Solid lines correspond to the refinement of the data with a global parameter set describing the CEF excitation at 4.5 meV, as described in the text; an example of the analysis is given in (b) with the different inelastic contributions marked by the gray-shaded areas.

extend these investigations to the $\boldsymbol{q}$-dependence and analyze the dispersion relation of the different modes. However, as the magnetic phase transition at T_{FE} is entirely driven by complex anisotropy terms [8, 40], the exchange parameters are similar for both magnetic phases [32] and we may focus on the discussion of the dispersion in the cycloid phase, where most data have been taken so far. Measurements have been performed at temperatures of 17 and 23 K in order to stay significantly above the ordering of the Tb moments. Nevertheless the Tb moments are already polarized by the Mn ordering and they may contribute to the scattering. It is, however, safe to exclude a significant role in the magnon dispersion which extends up to 9 meV in $TbMnO_3$.

4.1. Magnon dispersion in the ac plane: nearest-neighbor exchange

In the ferroelectric phase with cycloidal ordering the magnetic correlations in single $\boldsymbol{ac}$ planes are comparable with those of the commensurate A-type structure in the related rare-earth manganites with a less distorted crystal structure, such as e.g. $LaMnO_3$ [46]; along $\boldsymbol{a}$ the magnetic coupling is strictly ferromagnetic, and along $\boldsymbol{c}$ it is always antiferromagnetic [21]. Along $(q_h, 0.28, 1)$ the magnetic Brillouin zone thus extends from $q_h = -1.0 \cdots + 1.0$, and along $(0, 0.28, 1 + q_l)$ from $q_l = -0.5 \cdots + 0.5$ with respect to the $Pbnm$ lattice.

Figure 7 presents representative raw-data energy scans for different $\boldsymbol{Q}$ positions along the lines $(00.281 + q_l)$ and $(q_h, 0.28, 1)$ determining the magnon dispersion along $\boldsymbol{a}$ and $\boldsymbol{c}$ at $T = 23$ K. Considering the scans along $\boldsymbol{q} = (0, 0, q_l)$, figure 7(a) reveals how the different magnon branches propagate through the magnetic Brillouin zone. At the zone center, $q_l = 0$, the spectrum consists of three different excitations, see the discussion above, but in the spectra recorded using unpolarized neutrons shown in figure 7 the low-energy phason mode can only be anticipated as the broadening of the elastic response. The signal associated with the phason modes apparently rapidly merges with that of the low-frequency $\omega_{\perp_1}$ mode. Through the Brillouin zone, we may thus follow only two branches, but due to the use of unpolarized neutron scattering the associated characters cannot be fully analyzed. At the zone boundary, $q_l = 0.5$, magnon intensity is found near ≈4 meV and overlaps with the signal from the Tb-CEF excitation, which is visible in all spectra around 4.5 meV.

The superposition with the CEF excitation significantly hampers the determination of the magnon frequencies. However, the CEF signal is not expected to vary considerably, either in frequency or in spectral weight, within a single magnetic Brillouin zone [37]. Hence, a single parameter set for the description of the CEF parameter was applied in the fitting of the data, which allows us to determine the dispersion of the two spin-wave branches $\omega_{\perp_{1,2}}$. An example of the fitting of the data is given in figure 7(b).

In figure 7(c) we plot selected energy scans along the line $\boldsymbol{Q} = (q_h, 0.28, 1)$ aiming at the dispersion along $\boldsymbol{a}$. Again, the finite resolution prohibits the resolution of the phason mode, but two distinct magnon signals can be followed up to the magnetic zone center at $q_h = 1.0$. Along $\boldsymbol{a}$, the spin-wave signal extends to considerably higher energies than along $\boldsymbol{c}$ and crosses the CEF excitation at 4.5 meV. We stress again that the use of a global parameter set for the description of the CEF excitation allows the identification of the spin-wave intensities in the individual spectra.

The resulting spin-wave dispersion in the ferroelectric phase for $T = 23$ K within the $\boldsymbol{ac}$ plane is plotted in figure 8.

Table 2. Results of the analysis of the spin-wave dispersion using the simplified model described in the text, and comparison with the exchange constants obtained in different $RMnO_3$ compounds showing the A-type ordering. Note that different authors use different definitions of J and Λ. The values given have been converted to the Hamiltonian equation (9), which is the convention used in [47].

		J_{FM} (meV)	J_{AFM} (meV)	Λ (meV)	T_N (K)
$TbMnO_3$	Cycloid, $\omega_{\perp_1}$	0.10(1)	−0.37(3)	0.02(1)	42
	Cycloid, $\omega_{\perp_2}$	0.15(1)	−0.60(3)	0.11(2)	
$TbMnO_3$ [34]	Cycloid[a]	0.15	−0.50	0.13	42
$PrMnO_3$ [34]	A-type	0.56	−0.60	0.08	100
$LaMnO_3$ [48]	A-type	0.84	−0.61	0.15	140
$LaMnO_3$ [47]	A-type	0.83	−0.58	0.17	140

[a] Data presented in [34] were all recorded in the spiral phase at $T = 10$ K, the splitting of the magnon modes is not discussed.

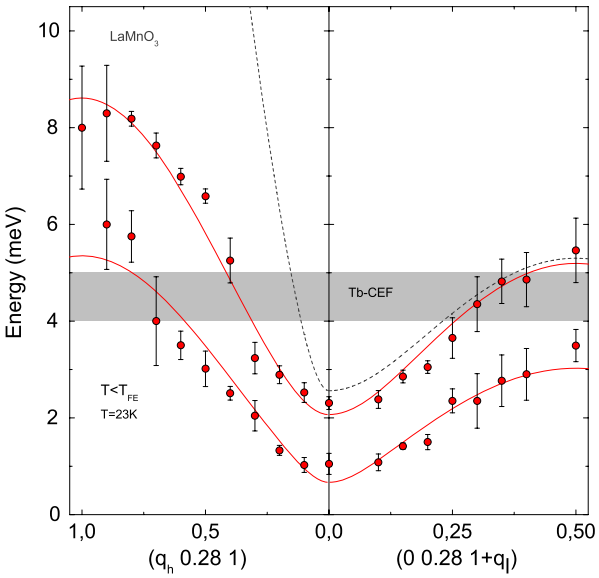

Figure 8. Spin-wave dispersion of the two orthogonal modes $\omega_{\perp_{1,2}}$ in the ferroelectric cycloid phase at $T = 23$ K along $\boldsymbol{a}$ and $\boldsymbol{c}$. Solid lines denote fits to the data as described in the text, dashed lines correspond to the magnon dispersion of $LaMnO_3$ as derived from the discussion in [47].

Starting from the zone center at $\boldsymbol{q} = 0$ the frequency of both $\boldsymbol{a}$-polarized modes continuously increases with increasing $|\boldsymbol{q}|$. Along $\boldsymbol{a}$ the maximum magnon energy amounts to ≈8 meV, which is much higher than the value of the zone-boundary frequency along $\boldsymbol{c}$ of ≈5.5 meV. As mentioned before, the magnetic correlations in the $\boldsymbol{ac}$ planes are similar to those in the commensurate A-type ordered $LaMnO_3$, and we may directly compare the observed spin-wave dispersion between both compounds. The magnon excitations in $LaMnO_3$ were first studied by Moussa *et al* and by Hirota *et al* [47, 48]. Based on a simple spin-only Hamiltonian

$$\mathcal{H} = -\sum_{i,j} J_{i,j} \boldsymbol{S}_i \boldsymbol{S}_j - \Lambda \sum_i S_i^{z2} \tag{9}$$

with a FM exchange J_{FM} between nearest neighbors within the $\boldsymbol{ab}$ planes, an AFM exchange J_{AFM} along $\boldsymbol{c}$, and a single-ion anisotropy Λ, the following spin-wave relations are derived [47]:

$$\hbar\omega(\boldsymbol{q}) = 2S\sqrt{A(\boldsymbol{q})^2 + B(\boldsymbol{q})^2}, \tag{10}$$

with $A(\boldsymbol{q})$ and $B(\boldsymbol{q})$ defined by

$$A(\boldsymbol{q}) = +2J_{FM}[2 - \cos(\pi(q_h + q_k)) - \cos(\pi(q_h - q_k))] - 2J_{AFM} + \Lambda,$$

$$B(\boldsymbol{q}) = -2J_{AFM}\cos(\pi q_l),$$

and $S = 2$ corresponding to fully ordered Mn^{3+} spin moments. This simple approach can, of course, not describe the splitting of the different magnon branches observed in $TbMnO_3$ with a single parameter set. However, these relations fit the observed $\boldsymbol{q}$-dependence of the single branches very accurately when different anisotropy terms and interaction parameters are introduced for the individual branches. The obtained values for the magnetic exchange interactions J_{FM} and J_{AFM}, and those for the single-ion anisotropies are summarized in table 2, and our results are in qualitative agreement with those of a previous neutron study by Kajimoto *et al* [34]. However, due to a relaxed resolution these authors do not report or analyze the splitting of the different magnon branches. The commensurate model used to describe the magnon dispersion perpendicular to the incommensurate modulation fully neglects the cycloidal character of the spin ordering in $TbMnO_3$ which furthermore is not circular but elliptical. In the first view this is justified, as for magnon propagation along the $\boldsymbol{a}$ and $\boldsymbol{c}$ directions the frustrating interaction along $\boldsymbol{b}$ does not enter. The different character of the two orthogonal modes $\omega_{\perp_{1,2}}$ arises from their different phase with respect to the $\boldsymbol{b}$ component of the static modulation. As a consequence, the in-phase and the $\frac{\pi}{2}$ branches experience different anisotropy energies as they flip essentially $\boldsymbol{b}$ and $\boldsymbol{c}$ moments respectively. Furthermore, the modes along the two directions perpendicular to the incommensurate modulation will retain their in-phase or $\omega_{\perp_{1,2}}$ character through the entire Brillouin zone. Since the cycloidal magnetic order is elliptical the two branches again experience different effective moments through the entire Brillouin zone, which in our fitting (10) results in individual interaction parameters. Both effects point to an identification of the lower branch with the $\frac{\pi}{2}$ modes, which at the zone center should couple strongest with the ferroelectric polarization. This mode is associated with the flip of the cycloid into the $\boldsymbol{a}, \boldsymbol{b}$ plane combined with the ferroelectric polarization flip into the $\boldsymbol{a}$ direction. The fact that this transition can be induced by moderate magnetic fields [45] further supports the interpretation that the $\frac{\pi}{2}$ mode has the lower energy. We may, however, not fully exclude that additional more complex interactions may overrule the argument given.

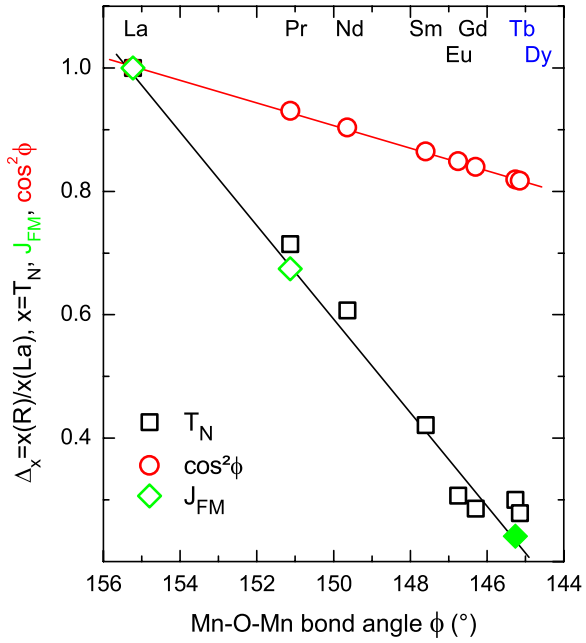

Figure 9. Néel temperature T_N, the ferromagnetic coupling J_{FM}, and $\cos^2\phi$ as a function of the average Mn–O–Mn bond angle ϕ in the series of rare-earth manganites $RMnO_3$. All values are normalized to those in $LaMnO_3$. Structural and magnetic data for the various compounds taken from the literature are denoted by open symbols [27, 28, 34, 47, 49, 50].

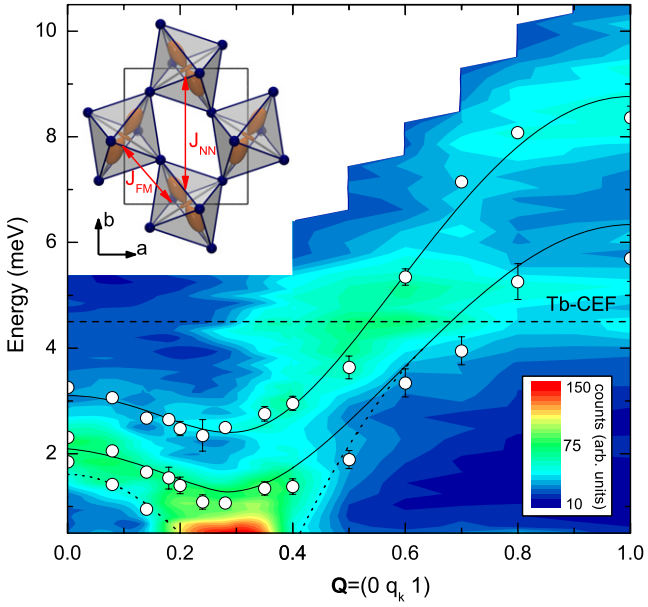

Figure 10. (a) Intensity mapping of the inelastic intensity for $T = 17$ K along the line $\boldsymbol{Q} = (0, q_k, 1)$ to unravel the magnon dispersion along [010], calculated from a grid of energy scans with step size $\Delta q_k = 0.1$. White areas were not accessible in the experiment. Open circles mark the estimated magnon frequencies; solid lines represent the fit of the estimated dispersion as explained in the text, dashed lines depict the contributions of the Tb-CEF excitation. Dotted lines are included as guides to the eye. The inset sketches the $\boldsymbol{ab}$ plane of the orthorhombic crystal structure highlighting the typical structural distortions of the $GdFeO_3$ type, the stable staggered orbital ordering, and the competing magnetic exchange pathways J_{FM} and J_{NN}.

The strength of the magnetic interaction parameters J_{FM} and J_{AFM} obtained for $TbMnO_3$ can be compared with those of $LaMnO_3$ exhibiting a less distorted orthorhombic structure. In figure 8 the magnon dispersion of $LaMnO_3$ is shown by the dotted lines. Along $\boldsymbol{c}$ the spin-wave dispersion is comparable for both compounds, and hence is the antiferromagnetic exchange J_{AFM}, see table 2. In contrast, along $\boldsymbol{a}$ the spin-wave dispersion is significantly flattened in the case of $TbMnO_3$; for $LaMnO_3$ the magnon bands extends up to ≈33 meV, whereas the zone-boundary frequency amounts to 8 meV in $TbMnO_3$, signaling the considerable weakening of the FM interaction J_{FM}. Indeed, the FM interaction is strongly suppressed, $J_{FM} \approx 0.15$ meV in $TbMnO_3$ and $J_{FM} = 0.83$ meV in $LaMnO_3$ [47], respectively.

In mean-field theory the Néel temperature T_N is closely correlated with the size of magnetic exchange interactions J. In figure 9 we plot the suppression of T_N in the series of rare-earth manganites $RMnO_3$ as a function of the average Mn–O–Mn bond angle. In addition we show the reported values of J_{FM} [34, 47, 48]. The linear decrease of T_N perfectly scales with the reduction of J_{FM}. The ferromagnetic correlations and the A-type ordering are destabilized by the enhancement of the structural distortion [28], resulting in the reduction of the bond angle ϕ. It is well established that T_N is closely coupled to $\cos^2\phi$ in the perovskite nickelates and ferrates [50–53]. In the series of rare-earth manganites the small difference in the bond angle is, however, not sufficient to fully explain the rapid suppression of T_N, see figure 9.

With the staggered orbital ordering the FM nearest-neighbor exchange J_{FM} in the $\boldsymbol{ab}$ plane can be parameterized as $J_{FM} = 4b^2/U$ with the on-site Coulomb repulsion U and $b \approx d^{-3.5}\cos\phi$ [54, 55]. The Mn–Mn distance d is almost constant in the $RMnO_3$-series [27], and in the simplest approach J_{FM} is solely determined by $\cos^2\phi$. However, the decrease in $\cos^2\phi$ does not describe the rapid suppression of J_{FM} and can only account for a small fraction of the observed decrease of J_{FM} and, consequently, of T_N. Note, that the AFM interaction along $\boldsymbol{c}$ is mediated by the isotropic t_{2g}^3–O–t_{2g}^3 exchange, which is almost independent of ϕ [52]. The observed rapid suppression of J_{FM} and T_N thus directly mirrors the influence of the orbital degree of freedom, and different approaches emphasizing the importance of orbital physics are needed in the manganites, as were proposed in the recent literature [49, 56].

4.2. Magnon dispersion along b: influence of magnetic frustration

The cycloid ordering in $TbMnO_3$ develops out of the A-type ordering in $LaMnO_3$ by a modulation of the magnetic correlations along [010] due to the emergence of the frustrating AFM interaction J_{NN} between next-nearest neighbors along $\boldsymbol{b}$ [28], see the inset in figure 10. The competition between J_{NN} with the nearest-neighbor exchange J_{FM} along the Mn–Mn bonds strongly affects the magnon dynamics, and the shape of the dispersion is significantly changed compared to the A-type structure along this direction.

In a first approach we treat the dispersion along $\boldsymbol{b}$ separately and expand the spin Hamiltonian equation (9) to include the AFM exchange J_{NN}. Calculating the Fourier components J_q results for $\boldsymbol{q}\|\boldsymbol{b}$ in the dispersion relation:

$$\hbar\omega(0q_k0) = 2S\Big(\big[2J_{\mathrm{FM}}\big(2-2\cos(\pi q_k)+\eta\cos(2\pi q_k)\big) - 2J_{\mathrm{AFM}} - 2J_{\mathrm{NN}} + \Lambda\big]^2 - 4J_{\mathrm{AFM}}^2\Big)^{\frac{1}{2}}, \tag{11}$$

with $\eta = J_{\mathrm{NN}}/J_{\mathrm{FM}}$. For small $|\eta| < 0.5$ the spin-wave dispersion increases continuously from the A-type zone center $q_k = 0$ to the zone boundary at $q_k = 1.0$, analogous to the dispersion along $\boldsymbol{a}$ already discussed. For larger η, however, the shape of the dispersion changes and develops a minimum at $q_{k0} = \arccos(-\frac{1}{2\eta})$: the static A-type ordering is destabilized and transforms into an incommensurable arrangement with modulation q_{k0} [57]. The observed value of the incommensurability ε_b yields a strong magnetic frustration of $\eta = -0.78$ in $TbMnO_3$, which is consistent with results from a mean-field calculation [28].

The observed dispersion along $\boldsymbol{Q} = (0, q_k, 1)$ for $0 \leqslant q_k \leqslant 1$ is shown in figure 10. The data were all acquired on a cold spectrometer with enhanced experimental resolution. For $q_k \leqslant 0.28$ the analysis of the data was supplemented by the results of the polarization study. This allows us to identify the three different magnon branches in the entire regime $0 \leqslant q_k \leqslant 0.28$. In the remaining part of the dispersion, we have to rely only on unpolarized data, which, unfortunately, does not allow us to fully separate the different magnon branches, and only the dispersion of the two $\boldsymbol{a}$ polarized electromagnon branches $\omega_\perp 1, 2$ can be resolved in this regime. Again, we expect the phason-mode intensity to rapidly merge with those of the other two branches. Starting from the A-type zone center $\boldsymbol{Q} = (0, 0, 1)$, all three modes exhibit a similar dispersion. With increasing q_k the frequencies of three modes soften towards the incommensurable Bragg position, and the dispersion reveals a clear minimum around $q_k = 0.28$ in the three branches. Upon a further increase the magnon energies rapidly increase and we find an upper cut-off energy of ≈8.5 meV at the zone boundary of the extended zone scheme at $q_k = 1.0$, similar to the maximum magnon energy along $\boldsymbol{a}$.

The observed $\boldsymbol{q}$-dependence is well described by the dispersion relation equation (11). Fixing the magnetic frustration $|\eta|$ to the value derived from the position of the incommensurable Bragg position, $|\eta| = 0.78$, the refinement of the data includes only the anisotropies Λ_i and the FM coupling J_{FM} as free parameters. Fitting the different branches independently, i.e. attributing the splitting of the modes to the complex magnetic anisotropy, we find a satisfying description of the observed data with $J_{\mathrm{FM}} = 0.11$ meV, in good agreement with the results obtained for the $\boldsymbol{a}$ and $\boldsymbol{c}$ directions.

5. Discussion of the electromagnon excitation

The good agreement between the frequencies of the two $\boldsymbol{a}$-polarized zone-center modes in the cycloidal phase at $T = 17$ K, revealed in our inelastic neutron scattering experiments, with the two frequencies obtained in the $\boldsymbol{a}$-polarized IR response strongly suggests the identification of the IR signal as the magnon. Since the chosen polarizations in the IR experiment would not allow for the detection of the magnetically $\boldsymbol{a}$-polarized mode via the magnetic field, the magnon must couple in the charge channel indicating its hybridized electromagnon character.

However the consideration of all the IR experiments performed for $TbMnO_3$ and $GdMnO_3$ [16], $Eu_{0.75}Y_{0.25}MnO_3$ [18] and $DyMnO_3$ [19] apparently disagrees with the simple electromagnon interpretation. Aguilar *et al* [18] first pointed out that the strong electromagnon response is always found along the $\boldsymbol{a}$ direction independently of the orientations of cycloid and polarization, while one expects the electromagnon polarization to follow the flop of the cycloid and static polarization. Furthermore, in the paraelectric phase in $TbMnO_3$, one would expect a strong electromagnon response to occur along the $\boldsymbol{c}$ direction along which the ferroelectric polarization develops below T_{FE} at zero field, but still the strong signal is only seen in the $\boldsymbol{a}$ direction [58]. Clearly an additional mechanism has to be taken into consideration to reconcile all these effects. Aguilar *et al* [18] suggested the two-magnon coupling as an alternative process, which Kida *et al* [19] also use to explain their $DyMnO_3$ spectra. Unfortunately, amongst the compounds studied by the IR measurements, inelastic neutron scattering experiments can only be easily performed for $TbMnO_3$ due to the strong neutron absorption of Gd, Dy and Eu. For $TbMnO_3$, however, there is good agreement concerning the frequencies at 17 K. It appears likely that the extracted IR frequencies correspond to a weaker sharp signal, the electromagnon, sitting on a broader possibly two-magnon activated feature. Furthermore, one must keep in mind, that the $\boldsymbol{a}$ and $\boldsymbol{c}$ directions in $TbMnO_3$ are fully different. The $\boldsymbol{a}$ direction corresponds to a [110] direction of the perfect perovskite and makes a 45° angle with the Mn–O bond, whereas the $\boldsymbol{c}$ direction points along the Mn–O bond. In consequence the phonon polarization patterns and frequencies are fully different along these directions. Since the electromagnon needs to get its weight from the higher frequency phonons a fully different situation can arise somehow favoring the response along the $\boldsymbol{a}$ direction.

6. Conclusion

In conclusion, we have presented a comprehensive analysis of the magnetic excitation spectrum in the multiferroic compound $TbMnO_3$. Ferroelectricity in $TbMnO_3$ is induced by a non-collinear cycloidal ordering. We have characterized the different spin-wave excitations in the cycloid structure both using unpolarized and polarized neutron scattering techniques. The lowest of the three different magnon modes observed at $\boldsymbol{q} = \boldsymbol{0}$ corresponds to the phason excitation of the cycloid structure, whereas the two other modes represent spin fluctuations perpendicular to the cycloid plane. One of these modes rotates the magnetic cycloid around its propagation vector and couples linearly to the electric polarization. This mode has the symmetry of the hybridized magnon–phonon excitation predicted to exist in magnetic ferroelectrics long ago [3, 4]. From the analysis of the full spin-wave dispersion it appears more likely that the lower of the two $\boldsymbol{a}$ polarized modes has the full electromagnon symmetry, but more

complex interactions as well as the elliptical and non-harmonic components of the order may modify and mix the characters of the two $\boldsymbol{a}$ polarized zone-center modes rendering them both IR active. There is a good agreement between the two frequencies recently observed using optical spectroscopy [16] and the two frequencies for the two $\boldsymbol{a}$ polarized modes in the cycloidal phase at $T = 17$ K; strongly suggesting the electromagnon character at least for the peak in the IR signal. The identification of the full IR response with the electromagnon is however still not unambiguous and two-magnon processes may play a role as well.

In the paraelectric phase the magnetic structure transforms into a collinear spin-density wave structure. The magnon spectrum of this phase consists of six different branches, which we have classified according to their relative phase with respect to the static ordering. While the branches with no phase shift retain the collinear spin arrangement and thus are not related to the magnetoelectric coupling, the transversal modes with out-of-phase character are relevant for the ferroelectric transition. These modes transform the SDW structure into a non-collinear cycloidal order and possess an electromagnon character even in the paraelectric phase. The $\boldsymbol{c}$ polarized mode associated with the cycloid confined to the $\boldsymbol{bc}$ plane condenses at the ferroelectric transition and can be identified with the associated soft mode of the multiferroic phase which is almost continuous.

The magnon dispersion of the different branches in the cycloidal phase is well explained within linear spin-wave theory. Along the $\boldsymbol{ac}$ plane the spin dynamics are governed by nearest-neighbor exchange interactions, and the comparison with the dispersion of $LaMnO_3$ [47] reveals a drastic suppression of the ferromagnetic interaction J_{FM} within the $\boldsymbol{ab}$ planes in the case of $TbMnO_3$. The splitting of the $\boldsymbol{a}$ polarized modes at $\boldsymbol{q} = 0$ remains sizeable throughout the Brillouin zone as the in-phase and out-of-phase characters with respect to the static $\boldsymbol{b}$ component do not vary when the magnon propagation vector is perpendicular to $\boldsymbol{b}$. The dispersion of the two branches can be described by two sets of anisotropy and effective interaction parameters. Along the $\boldsymbol{b}$ direction parallel to the modulation, the magnon spectrum is significantly influenced by the competition of J_{FM} with an antiferromagnetic nearest-neighbor exchange J_{NN}: the magnetic commensurate A-type ordering in $LaMnO_3$ transforms into the incommensurate ordering modulated along $\boldsymbol{b}$ due to the appearance of the frustrating next-nearest-neighbor exchange [28]. The spin dynamics fully agree with this picture and from the analysis of the dispersion relation we determine a strong magnetic frustration $J_{NN} \approx 0.80|J_{FM}|$ in perfect agreement with the mean-field analysis of the static modulation.

Multiferroic spiral magnets offer the possibility of obtaining a large mono-domain spiral magnet by applying an electric field. This opens new perspectives in inelastic neutron scattering as one may analyze the chiral components of the magnons as well as their dispersion.

Acknowledgments

We appreciate numerous valuable discussions with D Khomskii, M Mostovoy, N Nagaosa, and A Pimenov. The work at the University of Cologne was supported by the Deutsche Forschungsgemeinschaft through the Sonderforschungsbereich 608.

References

[1] Brown A D and Cowley R A 1981 *Structural Phase Transitions* (London: Taylor and Francis)
[2] Shirane G 1974 *Rev. Mod. Phys.* **46** 437
[3] Bar'yakthar V G and Chapuis I 1969 *Sov. Phys.—Solid State* **10** 2818
[4] Bar'yakthar V G and Chapuis I 1970 *Sov. Phys.—Solid State* **11** 2628
[5] Akhezier I A and Davydov L N 1971 *Sov. Phys.—Solid State* **12** 2563
[6] Smolenskii G A and Chapuis I E 1983 *Sov. Phys.—Usp.* **25** 475
[7] Katsura H, Nagaosa N and Balatsky A 2005 *Phys. Rev. Lett.* **95** 057205
[8] Mostovoy M 2006 *Phys. Rev. Lett.* **96** 067601
[9] Sergienko I and Dagotto E 2006 *Phys. Rev.* B **73** 094434
[10] Kimura T, Ishihara S, Shintani H, Arima T, Takahashi K H, Ishizaka K and Tokura Y 2003 *Nature* **426** 55
[11] Hur N, Park S, Sharma P, Ahn J, Guha S and Cheong S-W 2004 *Nature* **429** 392
[12] Lawes G *et al* 2005 *Phys. Rev. Lett.* **95** 087205
[13] Yamasaki Y, Miayasaka S, Kaneko Y, He J-P, Arima T and Tokura Y 2006 *Phys. Rev. Lett.* **96** 207204
[14] Heyer O, Hollmann N, Klassen I, Jodlauk S, Bohaty L, Becker P, Mydosh J A, Lorenz T and Khomsii D 2006 *J. Phys.: Condens. Matter* **18** L471
[15] Taniguchi K, Abe N, Takenobu T, Iwasa Y and Arima T 2006 *Phys. Rev. Lett.* **97** 097203
[16] Pimenov A, Mukhin A A, Ivanov V, Travkin V, Balbashov A and Loidl A 2006 *Nat. Phys.* **2** 97
[17] Pimenov A, Rudolf T, Mayr F, Loidl A, Mukhin A A and Balbashov A 2006 *Phys. Rev.* B **74** 100403
[18] Aguilar R V, Sushkov A B, Zhang C L, Choi Y J, Cheong S-W and Drew H D 2007 *Phys. Rev.* B **76** 060404
[19] Kida N, Ikebe Y, Takahashi Y, He J P, Kaneko Y, Yamasaki Y, Shimano R, Arima T, Nagaosa N and Tokura Y 2007 *Preprint* 0711.2733 [condmat]
[20] Sushkov A B, Aguilar R V, Park S, Cheong S-W and Drew H D 2007 *Phys. Rev. Lett.* **98** 027202
[21] Kenzelmann M, Harris A, Jonas S, Broholm C, Schefer J, Kim S, Zhang C, Cheong S-W, Vajk O and Lynn J 2005 *Phys. Rev. Lett.* **95** 087206
[22] Arima T, Tokunaga A, Goto T, Kimura H, Noda Y and Tokura Y 2006 *Phys. Rev. Lett.* **96** 097202
[23] Park S, Choi Y J, Zhang C L and Cheong S-W 2007 *Phys. Rev. Lett.* **98** 057601
[24] Cheong S-W and Mostovoy M 2007 *Nat. Mater.* **6** 13
[25] Kimura T, Lawes G, Goto T, Tokura Y and Ramirez A 2005 *Phys. Rev.* B **71** 224425
[26] Blasco J, Ritter C, Garcia J, de Teresa J, Perez-Cacho J and Ibarra M 2000 *Phys. Rev.* B **62** 5609
[27] Alonso J, Martínez-Lope M, Casais M and Fernández-Díaz M 2000 *Inorg. Chem.* **39** 917
[28] Kimura T, Ishihara S, Shintani H, Arima T, Takahashi K, Ishizaka K and Tokura Y 2003 *Phys. Rev.* B **68** 060403(R)
[29] Quezel S, Tcheou F, Rossat-Mignod J, Quezel G and Roudaut E 1977 *Physica* B **86–88** 916
[30] Kajimoto R, Yoshizawa H, Shintani H, Kimura T and Tokura Y 2004 *Phys. Rev.* B **70** 012401
[31] Argyriou D N, Aliouane N, Strempfer J, Zegkinoglou I, Bohnenbuck B, Habicht K and Zimmermann M 2007 *Phys. Rev.* B **75** 020101

[32] Senff D, Link P, Hradil K, Hiess A, Regnault L P, Sidis Y, Aliouane N, Argyriou D N and Braden M 2007 *Phys. Rev. Lett.* **98** 137206
[33] Aliouane N, Argyriou D N, Strempfer J, Zegkinoglou I, Landsgesell S and Zimmermann M 2006 *Phys. Rev.* B **73** 020102
[34] Kajimoto R, Mochizuki H, Yoshizawa H, Shintani H, Kimura T and Tokura Y 2005 *J. Phys. Soc. Japan* **74** 2430
[35] Zheludev A 2006 *ResLib 3.3* Oak Ridge National Lab
[36] Brown P J 2004 Magnetic form factors *International Tables for Crystallography* vol C 454ff (Dordrecht: Kluwer–Academic)
[37] Fulde P and Loewenhaupt M 1986 *Adv. Phys.* **34** 589
[38] Moon R M, Riste T and Koehler C 1969 *Phys. Rev.* **181** 920
[39] Katsura H, Balatsky A V and Nagaosa N 2007 *Phys. Rev. Lett.* **98** 027203
[40] Nagamiya T 1967 Helical spin ordering—1. Theory of helical spin configurations *Solid State Physics* vol 20 (New York: Academic) p 305ff
[41] Goto T, Kimura T, Lawes G, Ramirez A and Tokura Y 2004 *Phys. Rev. Lett.* **92** 257201
[42] Marshall W and Lovesey S W 1971 *Theory of Thermal Neutron Scattering* (Oxford: Clarendon)
[43] Akhezier A I, Bar'yakhtar V G and Peletminskii S V 1968 *Spin Waves* (Amsterdam: North-Holland)
[44] Chupis I E 2007 *Low. Temp. Phys.* **33** 715
[45] Senff D, Link P, Aliouane N, Argyriou D N and Braden M 2008 *Phys. Rev.* B **77** 174419
[46] Wollan E O and Koehler W C 1955 *Phys. Rev.* **100** 545
[47] Moussa F, Hennion M, Rodríguez-Carvajal J, Moudden H, Pinsard L and Revcolevschi A 1996 *Phys. Rev.* B **54** 15149
[48] Hirota K, Kaneko N, Nishizawa A and Endoh Y 1996 *J. Phys. Soc. Japan* **65** 3736
[49] Zhou J-S and Goodenough J B 2006 *Phys. Rev. Lett.* **96** 247202
[50] Dabrowski B, Kolesnik S, Baszczuk A, Chmaissem O, Maxwell T and Mais J 2005 *J. Solid State Chem.* **178** 629
[51] Boekema C, ven der Woude F and Sawatzky G A 1972 *Int. J. Magn.* **3** 341
[52] Zhou J-S and Goodenough J B 2003 *Phys. Rev.* B **68** 054403
[53] Zhou J-S and Goodenough J B 2003 *Phys. Rev.* B **68** 144406
[54] Anderson P W 1950 *Phys. Rev.* **79** 350
[55] Rodríguez-Carvajal J, Hennion M, Moussa F, Moudden A H, Pinsard L and Revcolevschi A 1998 *Phys. Rev.* B **57** R3189
[56] Kim W S, Moon S J, Jung J H, Yu J, Parashar S, Murugavel P, Lee J H and Noh T W 2006 *Phys. Rev. Lett.* **96** 247205
[57] Konstantinidis N P and Patterson C H 2004 *Phys. Rev.* B **70** 064407
[58] Pimenov A 2008 private communication